




Image-Based Diagnostic System for the Measurement of Flame Properties and Radiation

Frédéric Morandini* , Tom Toulouse, Xavier Silvani, Antoine Pieri and Lucile Rossi, CNRS, UMR 6134 SPE, Campus Grilmedi, Université de Corse, 20250 Corte, France

Received: 5 November 2018/**Accepted:** 11 May 2019

Abstract. Data collection in the field is fundamental in providing relevant information during fire spread across vegetation or in industrial environments. Considering the challenge and costs of obtaining measurements in the presence of a fire at such a large scale, the development of non-intrusive optical methods is a good alternative. As part of an ongoing effort to improve the understanding of wildfire spread and provide useful tools for fire management, an image-based diagnostic system is being developed for the three-dimensional reconstruction of the turbulent flame in the field. The method allows the time-resolved measurement of the geometric flame features (height, surface area and volume). This paper presents the application of two synchronized stereovision systems to static line of fire scenarios. Each stereovision system, with 1 m inter-camera distance, was located at 12 m from the fire and captured complementary images from front and rear views. Dual spectral band (visible-NIR) cameras were used to enhance fire pixel detection. A series of experiments were carried out on 5 m long and 2 m wide beds of excelsior in the open with fuel loads of 2, 4 and 8 kg/m². The maximum flame heights were in the range of 1.2–2.4 m. Measurement of the heat flux densities was performed at several positions using thermopile-type sensors. Peak heat fluxes of 6.4–15.7 kW/m² were measured at 3 m from the fire. The thermal radiation impinging ahead of the flame front was characterized according to its geometric properties. The results exhibit not only a linear relationship between the flame volume and radiant heat flux but also high correlations between their temporal fluctuations. The image processing technique enables measurements of flame volume to be a reliable substitute for the usual fire thermal properties.

Keywords: 3D flame reconstruction, Stereovision, Flame volume, Flame surface, Radiant heat flux

1. Introduction

If early detection and extinguishment of a small fire that could have been suppressed using simple ground fire extinguishing methods fail, the fire can turn into an *uncontrollable* wide-spreading fire that makes the success of firefighting actions

* Correspondence should be addressed to: Frédéric Morandini, E-mail: frederic.morandini@univ-corse.fr



very difficult, even with air support. Generally, the few wildfires that escape containment account for the near totality of burned areas [1] driven by extreme weather conditions across landscapes with years of vegetative fuel accumulation. With climate change, large and severe fires have increased in occurrence, duration and intensity the last decade [2–4]. The last catastrophic events have occurred in recent years, causing the worst wildfire seasons on record in many counties all over the world such as Portugal, Spain, France, Italy, Greece, Chile, California Canada or Australia [5, 6]. These devastating fires, involving a wide range of spatial and temporal scales, dramatically result in human injuries or fatalities [7–9] and huge ecologic, economic and societal damages. These fires burn vegetation and houses and force people to leave their threatened homes, as well as cause soil erosion, air pollution, and negative consequences on water quantity and quality [10–13].

The real-time evaluation of the power of fires spreading in the open and the associated potential thermal damages is essential for both fire suppression purposes and the fundamental understanding of fire behavior. The knowledge of fire properties (thermal and characteristic length scales) can provide information apt to assist fire management activities. For instance, it can determine the amount of water for suppression or the effectiveness of a fire retardant drop at strategic locations [14–19]. The heat release rate (HRR) is the best variable for characterizing fire properties and consequent hazards [20]. However, the accurate measurement of the HRR during a fire spread requires oxygen consumption calorimetry, which can only be performed within a laboratory at small scales [21, 22]. The absence of an instrument to directly measure fire intensity in the field has made it necessary to develop alternative methods to characterize fires. Transducers, such as thermocouples, provide local measurements of temperature but such intensive physical variables provide information of lesser value if the sensor density is low. The spatial distribution of these quantities must be sufficiently resolved in order to assess heat transport phenomena. A more relevant approach consists of the measurement of integral quantities, such as heat flux densities emitted from a flame front during fire spread because the heat fluxes are closely related to the fire spread and rate of heat release [23–26]. More particularly, the measurement of thermal radiation from the flame front, which plays a significant role in the spread of fire, is of great importance in fire safety studies. However, sensors perform only point measurements of the line of fire and are distance-limited. The main issue with fires is that they create a very harsh thermal environment for most of the measurement devices. Additionally, wildfires are hardly accessible for performing in situ event measurements. To obtain information on these fires in the open, some relationships or rules of thumb based on simple observations of the geometric properties of flames were developed *for operational use* in the field [27, 28]. Because of their relatively easy estimation, the flame height and length are the parameters that were extensively studied to characterize the dynamics of turbulent flames. Numerous flame height correlations using dimensionless scaling parameters were derived from experimental data [29–34] and the HRR can be estimated from inverse modelling based on image recognition technique [35]. Although radiation from flames is a complex volumetric mechanism, simplified models were elaborated to predict

fire safety distances using flame height assuming flame front as a radiant surface [36–41]. Predictions of radiant heat flux according to the distance to the fire were also performed considering a radiative surface of an assumed shape [42–46].

The difficulty of wildfire instrumentation in the field renders remotely sensed data collection from optical systems a useful resource to determine quantitative fire properties. Flame detection, monitoring or measurements from cameras have received increasing attention from the fire science community in recent years thanks to their remote sensing capability over large spaces and long-time scales. Various processing methods were applied to fire images recorded over different spectral ranges from visible light to infrared light [47–51]. Near infrared (NIR) cameras are a good substitute to infrared cameras because they cost less and intrinsically offer great fire detection abilities, even under smoke conditions [52–54]. The binary image segmentation, which is the partitioning of the images into fire and background components, is also easier and more efficient with these cameras compared to color image ones. Image processing is usually performed to determine the basic flame geometric features but fire science and management benefit more from the estimation of fire thermal properties such as heat fluxes [55] or HRR [56–58].

Forty years ago, the measurement of turbulent flame shapes presented a major challenge to experimentalists [59], but recently, excellent progress has been made in image processing. The three-dimensional reconstruction of a flame is now possible using several cameras capturing complementary images of the fire from different view angle [60–62]. Mason et al. [55] extracted flame presence probability data from time-averaged sequences of binary images and estimated a mean 3D flame surface. They proposed an innovative technique for the evaluation of the thermal radiation fields surrounding a flame from shape factor and emissive power assumption, that has been demonstrated to be accurate on a steady burner flame. Previously Toulouse et al. [53] presented a method for measuring instantaneous 3D features of an unsteady flame front using two synchronized multimodal stereo-vision systems consisting of color and NIR cameras. A new fire detection algorithm based on multispectral images and multisensory data fusion was detailed. This algorithm allows for a more robust extraction of fire regions from the background. The image processing technique is not based on the mean of a large set of frames and puffing behavior of the turbulent flame is taken into account by the processing of each instantaneous frames. In the present paper, this technique is applied to static fire experiments close to real-world scenarios. The objective of this work is to provide an accurate measurement of the geometric properties (surface area and volume) of a puffing flame in order to provide an estimation of fire thermal properties such as radiation fields.

2. Materials and Methods

2.1. Static Fire Experiments

The static fire experiments presented in this study were designed to produce turbulent flame at an intermediate scale, representative of those observed during wild-

fire spread across scrublands. The fuel consisted of a 5 m long and 2 m wide bed of excelsior (Fig. 1), and the fuel loads ranged between 2 kg/m^2 and 8 kg/m^2 in order to vary the power of the fires. Five fire tests were conducted in the open, and the properties of the fuel bed are detailed in Table 1.

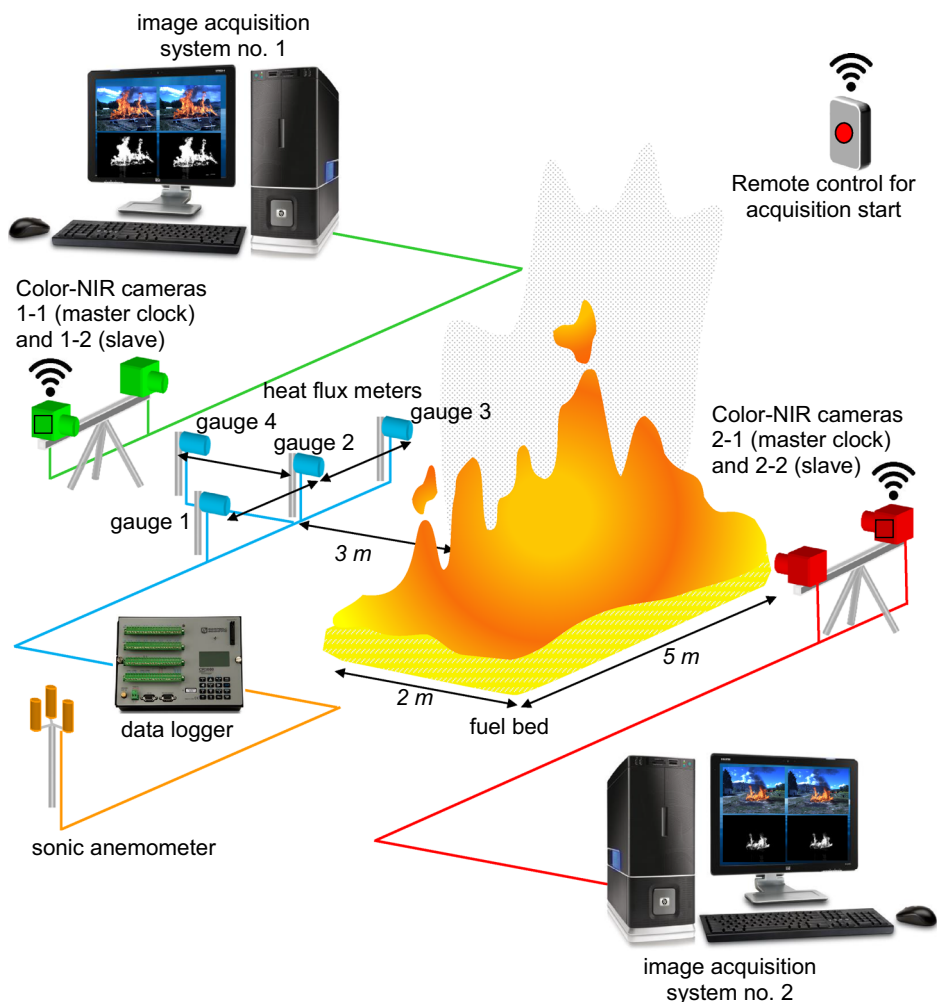


Figure 1. Experimental setup used for static fire tests over beds of excelsior in the open. Two stereovision systems, composed of four cameras, were positioned to obtain complementary front and rear views of the fire. Radiant heat flux measurements were performed at several positions using four thermopile-type sensors. A two-dimensional ultrasonic anemometer recorded the wind velocity and direction.

Table 1
Test Configurations and Average (Standard Deviation) Fire Properties

Test no.	Fuel load (kg/m ²)	Wind (m/s)	Bed height (m)	Quasi-steady (s)	Flame height (m)	Heat flux ^a (kW/m ²)
2_1	2	2.7 (± 1.1)	0.45 (± 0.06)	28	0.85 (± 0.25)	5.35 (± 1.33)
2_2	2	3.4 (± 1.3)	0.50 (± 0.07)	55	0.65 (± 0.25)	4.40 (± 0.83)
4_1	4	4.2 (± 1.3)	0.55 (± 0.07)	36	0.90 (± 0.35)	6.55 (± 1.05)
4_2	4	3.6 (± 1.6)	0.58 (± 0.08)	54	1.15 (± 0.45)	9.17 (± 3.06)
8_1	8	2.3 (± 1.1)	0.66 (± 0.09)	117	0.90 (± 0.20)	6.57 (± 0.43)

^aHeat flux measured at 3 m along the centerline axis of the flame front (gauge 2)

2.2. Wind and Heat Flux Measurements

A two-dimensional ultrasonic anemometer recorded the wind velocity and direction. The anemometer was located 2.0 m above the ground surface to measure the average horizontal wind acting on the fire front and on the downwind side of the fuel bed to minimize its influence on the wind measurements. Furthermore, such a placement prevented the smoke and large-diameter firebrands generated by the fire, which affect sonic measurements, from reaching the ultrasonic transducers.

The radiant heat fluxes emitted from the flame front during the fire spread were measured using 4 Schmidt-Boelter thermopile-type sensors (64 series from Medtherm Corporation, Huntsville, AL, USA). These transducers were calibrated by the manufacturer against a radiant reference in the range of 0–20 kW/m² with a calibration uncertainty of ± 2%. The gauges have a repeatability of ± 0.5%, a maximum non-linearity of ± 2% of the full range and a response time less than 0.25 s. A Sapphire window attachment, with a useful transmittance range of 0.2–5.5 μm, was added on the gauges to eliminate the convective heat transferred to the sensing area. The wide-angle (150°) transducers were oriented toward the fire to view the entire flame front. A thermocouple recorded the body temperature of the gauge. Considering the previous experiments conducted on similar beds the upper measurement threshold (20 kW/m²) is usually reached at about 2 m from the fire. In order to avoid saturation of the transducers output signal, the gauges were thus located at 3 m and 4 m from the fuel bed edge at a height of 1 m (Fig. 1). This location also prevents them from being impinged by flames for a long duration in case of wind gust. The measurements were recorded using a data logger (CR3000 from Campbell Scientific Ltd., Shepshed, Loughborough, UK) at a sampling rate of 1 Hz.

2.3. Fire Geometric Characteristics Measurements

The vision framework was composed of two identical stereovision systems, deliberately positioned to obtain complementary views of the fire front. The distance from the fire was approximately 12 m (Fig. 1). Each system was made with two multispectral cameras (JAI AD-080GE) rigidly fixed on a metallic bar and spaced 1 m apart (baseline length). Each camera simultaneously acquires two images, in

the visible and NIR (700–900 nm) spectral bands, through the same lens. The resolution of the cameras was 1024×768 pixels (with a 1/4-inch sensor and pixel size of $4.9 \mu\text{m}$). The cameras were equipped with a 6 mm focal length lens and their frame rate can reach up to 25 frames per second. In the present study, image acquisition was performed at 1 Hz. The bimodal approach developed by Toulouse et al. [53] combines both visible and NIR channels to efficiently reduce the masking effects of the flame front by the smoke. The data fusion enhances the accurate estimation of the fire volume as a radiant source. Because the visible images are used as reference for many studies working on fire problems, the use of this camera is optimal to process multimodal images and detect fire pixels by data fusion. Camera image acquisition was started using a radio remote control. The radio signal received by the system receiver was converted into a Transistor–Transistor Logic (TTL) output signal. This signal is sent to the trigger input of both cameras configured in the master (clock) and slave mode. The cameras continuously acquire synchronized images at the frequency set by a pulse generator. The acquisition was controlled by a Nuvo-1000 system integrating a Gigabit Ethernet controller (Intel® 82574 L). The images are stored in RAW format and later processed for segmentation and three-dimensional reconstruction.

The stereovision systems were calibrated in the field just before each experiment using a $1 \text{ m} \times 1 \text{ m}$ checkerboard with square patterns. The calibration is a procedure that permits the estimation of intrinsic and extrinsic parameters used in the stereo image rectification process. To accurately project the three-dimensional fire points computed from the images acquired by the two stereovision systems in the same frame, it is necessary to have the precise position, inclination and orientation of each vision system. A centimeter-precision GPS system was used (Leica Viva CS10 receptor with RTK) to obtain their positions. During the experiments, the precision varied from 2 cm to 5 cm according to satellite positions. Because the framework must be able to perform on any terrain topology and experimental configuration, the stereovision devices can be inclined and an Inertial Measurement Unit (IMU) was used to estimate their roll, pitch and yaw. To reduce the measurement errors of the IMU and GPS, their data were acquired for 2 min, and the averages of the data were used as the measure of the location and angular position of the systems. These data were used in the three-dimensional point registration process.

The whole procedure for measurements of fire geometric characteristics was fully described in [53] and can be summarized as follows. The first step consists of the detection of fire pixels using the information obtained in both the visible and NIR spectral bands. Then, the most significant feature points to be used in the stereo matching algorithm are selected. From these corresponding points, a triangulation procedure permits their projection in the three-dimensional space. The projection of the data from each stereovision system is achieved using multisensory data fusion based on cameras, GPS and IMU data. Finally, the reconstruction of the three-dimensional model of the flame front is performed and its geometrical characteristics (height, H_f , surface area, S_f , and volume, V_f) are computed.

2.4. Measurement Uncertainty of the Flame Volume

The uncertainty for the measurement of volumes using stereo vision is difficult to quantify, particularly for reactive gases with no solid surface. The estimation of the resulting uncertainty is not feasible for such complex shapes such as flame because of the way the error of each individual point used to reconstruct the volume propagates through the entire multimodal stereovision process. Nevertheless, the global uncertainty mainly depends on the accuracy of the correlation match (based on the image texture) and on geometrical parameters (measurement distance, distance between the two cameras and the lens' focal length). The main problem is not in determining the correspondence of the pixels in the images from the right and left cameras but in determining depth accuracy. The difference between the right and left images (disparity) decreases with increasing distance and the location of the stereovision systems were optimally determined considering the previous intrinsic and extrinsic parameters. The stereo vision calibration process, consisting of acquiring and processing multiple stereo pairs of a known pattern (checkerboard) within the measurement distance range (12 ± 1 m), minimizes the pixel correspondence error. However, some errors can nevertheless occur when measuring objects in the scene. The uncertainty along the longitudinal axis (depth), Δz , is given by:

$$\Delta z = \frac{z^2}{B f} \Delta d \quad (1)$$

where Δd is the disparity uncertainty in pixels (< 1 px), z is the real distance between the object and the stereovision system (12 m), B is the baseline (1 m), and f is the focal length of the cameras in pixels (1224 px). For the present configuration, the expected depth uncertainty is approximately 0.13 m. To evaluate the overall relative uncertainty in the estimation of the volume, $\frac{\Delta V}{V}$, incorporating the entire contribution of the different system parameters, a comparison of the measurements to the characteristic lengths of a reference object (a car) at the same distance was performed [53]. The relative uncertainty was evaluated to be below 14%, which is acceptable considering the complex shapes of flames.

3. Results and Discussion

The wide edge of the excelsior beds was lit using alcohol and a fire torch. An ignition line was performed when wind speed was low (< 5 m/s) in order to minimize inertial forces and obtain a nearly vertical flame front. Table 1 lists the test configurations for the entire set of experiments and mean fire properties. Due to both the high surface-to-volume ratio of excelsior and the porous properties of the fuel layer, the fire grew at a fast rate. A quasi-steady 5-m long flame front, governed by buoyancy (low Froude number), developed above the fuel layer after a few seconds (Fig. 2). The maximum flame heights and peak heat fluxes were in the range of 1.2–2.4 m and 6.37–15.69 kW/m², respectively, according to the fuel load. These geometric and radiative properties of the flames from the excelsior fuel bed

were representative of wildfires measured in the field [25, 63]. Nevertheless, the power of the fire increased with increasing fuel load up to an extent. Increasing the fuel load over 4 kg/m^2 resulted in a bed of fuel with a much higher bulk density. For the 8 kg/m^2 fuel load configuration, instead of a homogeneous combustion zone over the full depth of the fuel bed, a pyrolysis front spreading inside the fuel layer was observed, and a substantial increase in the flame residence time was also observed.

The post-processing of the images recorded by the four multispectral cameras was performed following the method detailed in [53]. The algorithms for flame detection, image segmentation and flame geometric property measurements were applied successfully to each of the fire image sequences. Figure 3 shows an example of the synchronized multimodal images acquired by the two vision systems. The resulting three-dimensional reconstruction of the flame front from these images is displayed in Fig. 4. It is worth mentioning that the knowledge of the flame shape is increasingly required for the evaluation of fire hazards, flame volumetric rate of heat release, fire radiation heat transfer, flame radiative feedback or flame emissivity (extinction coefficient and its associated path-length). Without the



Figure 2. Photograph of a static fire experiment over 5 m long and 2 m wide beds of excelsior in the open (Fire Test 4_1). The wide edge of bed was lit using alcohol and a fire torch. The resulting maximum flame height was in the range of 1.2–2.4 m.

appropriate tools and methods to measure its shape accurately, the flame is usually assumed as a simplified geometric shape, such as a cuboid [26], a cone [64, 65], a pyramid [59], a cylinder [41, 43, 45], cylindrical at each height [44, 64], a triangular prism [66] or a cylinder-cone combined shape [42, 46]. However, information loss is inevitable when assuming a general flame shape and such techniques are not applicable to non-symmetric flames. Furthermore, although radiative energy emission from reactive gases is a volumetric phenomenon, the flame front is often considered as a radiant surface using the solid-flame approach [36–40, 42, 46]. Considering the need for flame shape measurements in fire science, the present methodology provides interesting perspectives.

The temporal evolution of the properties of the buoyancy-driven flame was measured for the entire set of experiments. The time-history of the flame height, flame surface area, flame volume and heat fluxes densities are provided in Fig. 5

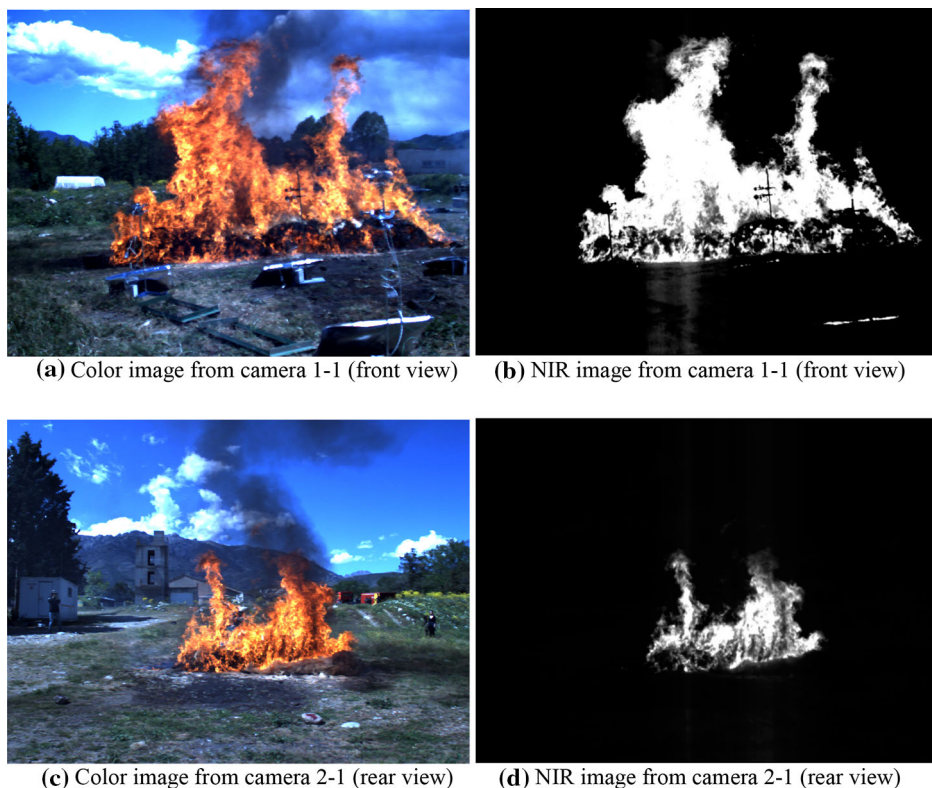


Figure 3. Images captured synchronously by two of the four cameras during Fire Test 4_1 at time 15 s. Each camera simultaneously acquires two images, in the visible and NIR spectral bands, through the same lens. Front view from camera 1-1: (a) color and (b) NIR images. Rear view from camera 2-1: (c) color and (d) NIR images (Color figure online).

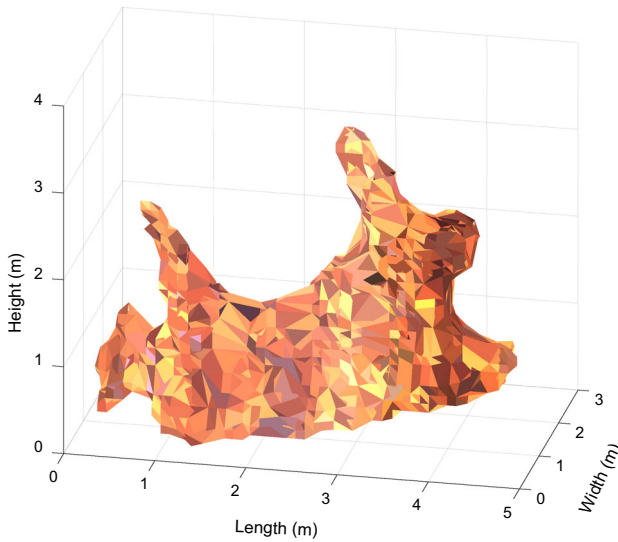


Figure 4. Three-dimensional reconstruction of the flame at time 15 s for (Fire Test 4_1). The most relevant fire pixels detected in multimodal images are projected in the three-dimensional space using a triangulation procedure. The reconstruction of the model of the flame front is performed and its geometrical characteristics (height, H_f , surface area, A_f , and volume, V_f) are computed.

(color curves) for Fire Test no. 4_1. In contrast to static fires from gas fed burners where a constant flow rate of fuel can be maintained during long periods, the experiments on a bed of fuel are characterized by the following 3 stage process that clearly appears in all the measured quantities due to the consumption of the fuel material. After ignition, a very sharp increase in all measured quantities is observed during the short fire growth stage (< 10 s). In all the experiments, the fire properties reached a quasi-steady state with fully developed flames from 17 s to 127 s (Table 1) according to fuel load and wind velocity and then decreased slowly. During this stage the average flame surface area to volume ratio was nearly constant (9.3 ± 0.9 1/m) for the present fire line configuration. Furthermore, the flame from vegetative fuels at field scale exhibited turbulent behavior with fluctuating features (puffing flames) due to the competition between the upward buoyancy forces generated by the fire and the induced lateral air entrainment. Each raw time series $\phi_i(t)$ (flame height, H_f , flame surface area, A_f , flame volume, V_f and radiant heat flux, \dot{q}_r'') can be expressed as a sum of a trend component and a fluctuating component [67] as follows:

$$\phi_i(t) = \overline{\phi_i}(t) + \phi'_i(t) \quad (2)$$

A moving average method using a length of 7 s was used to estimate the main trend-cycle (black curves in Fig. 5) and remove these fluctuations, which are fur-

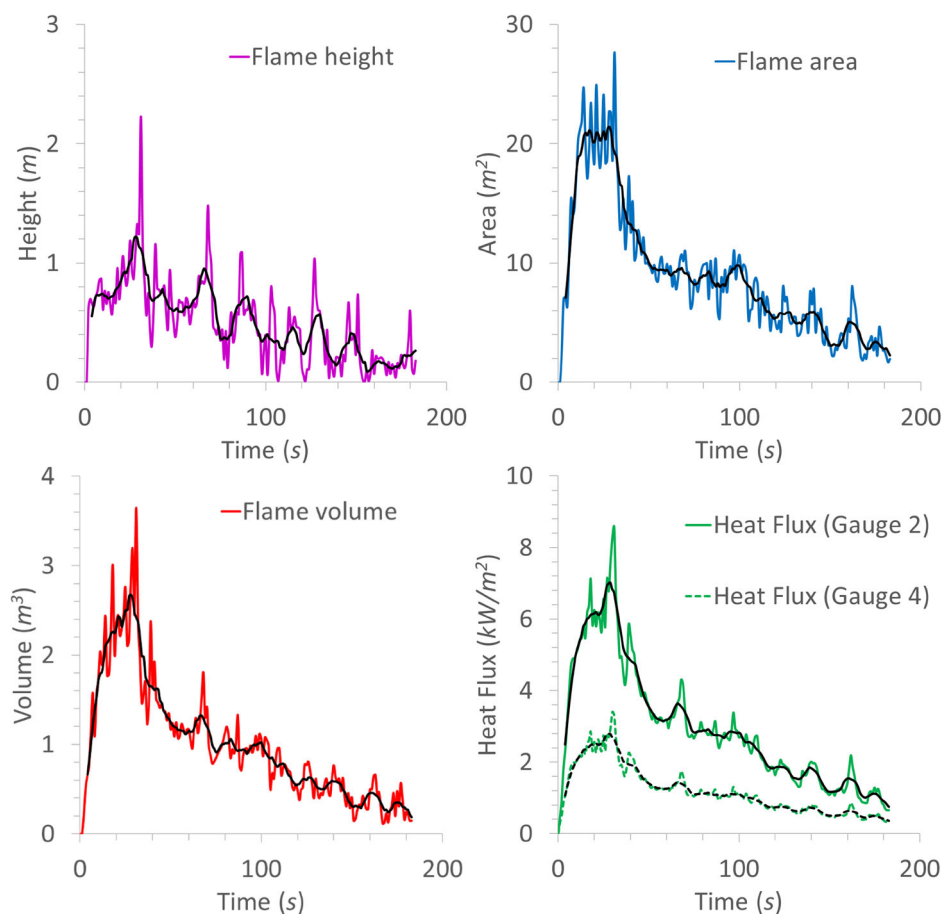


Figure 5. Time-history measurements of the (a) flame height, (b) flame surface area, (c) flame volume and (d) heat fluxes for Fire Test 4_1. The instantaneous data are plotted in colors and the 7 s moving average in black (Color figure online).

ther examined in the following paragraph. The moving average window was chosen as the shorter period that remove the short-term fluctuations from the data without introducing a spurious long-term trend. Furthermore, whatever the quantities and fuel load, the long term trends spread over more than 70 s. Averaging the data over a period of 7 s ensures that the fluctuations are averaged over a period significantly shorter than the long-term time scale of the fire. The relationships between the averaged variables are examined. Only the data points from after the growth stage were considered because charring materials begin to appear when the fire is fully developed, increasing radiant heat transfers ahead of the flame front. Figure 6 displays the scatterplots between pairs of parameters (flame geometric variables and heat fluxes measured at two different locations). These scatterplots

suggest the existence of linear relationships between some variables. The least squares regression method was used to find the line that *best fits* the data. The linear regression coefficients and coefficients of determination are provided in Table 2 for each fire configuration. For the range of experiments considered, the flame volume appears to be the variable that is best correlated with the radiant heat flux ($R^2 > 0.91$). The linear regression fit suggests a constant flame volumetric emissive power. The flame front surface area also presents good correlations ($R^2 > 0.83$). Furthermore, for the present flame front topology, such as those encountered during a fire spread in the open, the average flame height is not the most relevant parameter to study since large discrepancies exist along the line of

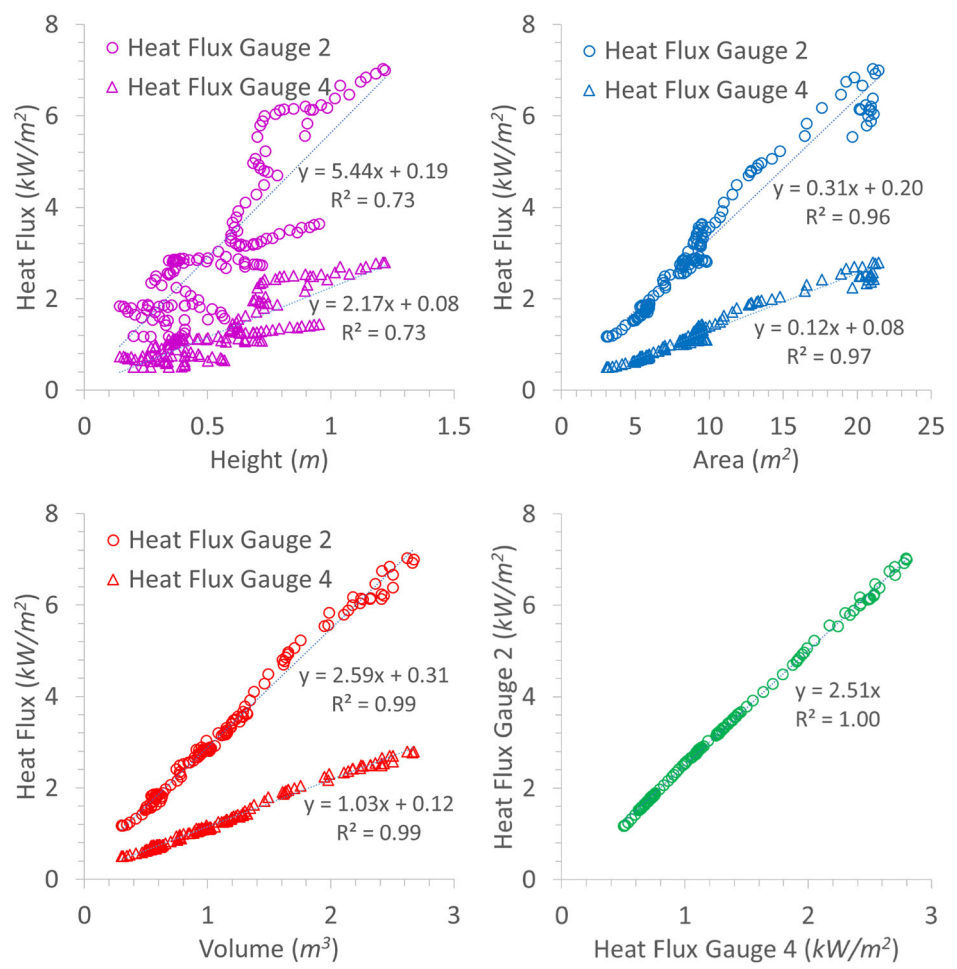


Figure 6. Linear (least squares) regression between flame geometric variables (height, surface area and volume) and heat fluxes for Fire Test 4_1. The flame volume appears to be the variable that is best correlated with the radiant heat flux ($R^2 = 0.99$).

Table 2
Linear Regression Coefficients (and Coefficients of Determination) for the Relationship Between Flame Geometric Variables (Height, Surface Area and Volume) and Heat Flux Measured at 3 m Along the Centerline Axis of the Flame Front (Gauge 2)

Test no.	Height (kW/m ² /m)	Area (kW/m ² /m ²)	Volume (kW/m ² /m ³)
2_1	5.97 ($R^2 = 0.71$)	0.29 ($R^2 = 0.90$)	2.77 ($R^2 = 0.92$)
2_2	5.71 ($R^2 = 0.67$)	0.30 ($R^2 = 0.95$)	2.79 ($R^2 = 0.97$)
4_1	5.44 ($R^2 = 0.73$)	0.31 ($R^2 = 0.96$)	2.59 ($R^2 = 0.99$)
4_2	4.81 ($R^2 = 0.79$)	0.32 ($R^2 = 0.94$)	2.91 ($R^2 = 0.96$)
8_1	7.61 ($R^2 = 0.77$)	0.30 ($R^2 = 0.83$)	2.74 ($R^2 = 0.91$)

fire (Fig. 3). This characteristic length scale would thus be more appropriate for axisymmetric flame configurations [29, 34, 68–70]. These results suggest that radiative heating impinging ahead of a flame front can remotely be estimated from flame volume measurements. In the present experimental configuration, optical and radiation measurements were performed at 12 m and 3 m from the fire, respectively. Peak heat flux measurements exhibit values greater than the maximum allowable exposure for skin at 4.7 kW/m² [66], whereas optical measurements were performed at a safer distance. The perfect linear relationship ($R^2 = 1$), observed between the radiant heat flux measured from the different gauges illustrates the attenuation of radiation with distances from the fire (Fig. 6). For the range of heat fluxes considered in the present study (0–15.7 kW/m² at 3 m from fire) the average regression coefficients for the flame surface area and volume are 0.30 ± 0.01 kW/m²/m² and 2.76 ± 0.11 kW/m²/m³, respectively. These regression coefficients are not dependent on the fuel load since the regression coefficients exhibit low standard deviation over the full set of experiments. Nevertheless, they are able to vary depending on the fuel or flame emissivity. It should be noted that the flame volume (or surface area) and the radiant heat flux impinging ahead of the fire are not strictly proportional. The y-intercept of the best fit line does not pass through the origin due to the presence of charring materials that shift the curve upward.

The previous simple regression analysis indicates the relationship between some of the moving time-averaged geometric properties of the flame front and the radiant heat flux. However, additional information can be obtained by processing the data further. The decomposition of the measured quantities into the additive time series (Eq. (2)) allows to better assess the reliability and accuracy of the three-dimensional imaging technique on flames. An example of the trend and fluctuation components of the volume and radiant heat flux is provided in Fig. 7 for Fire Test no. 2_2. The amplitude of the fluctuation components (flame surface area, volume and heat flux) is substantially different during the 3 flame stages (growth, development and decrease) but these time series can be considered stationary during the development flame stage. The amplitude of the fluctuation components was also observed to increase with increasing fuel load during this stage. Although

the vision system has the capability to measure at 25 Hz, the sampling rate used in this exploratory study was only 1 Hz and unfortunately, the effect of the fuel load on the flame puffing frequency could not be examined more thoroughly. The Pearson product-moment correlations between the fluctuations of the flame geometric variables (surface area and volume) and radiant heat fluxes were calculated. The correlation matrix for the full set of experiments is displayed in Table 3. The correlations for Fire Test no. 4_2 were slightly lower than those observed during other tests due to the higher variability in wind speed and direction during the experiment. Despite the relatively high estimated uncertainty of the volume measurements (14%), the fluctuations of the flame volume are highly ($r > 0.7$ in most

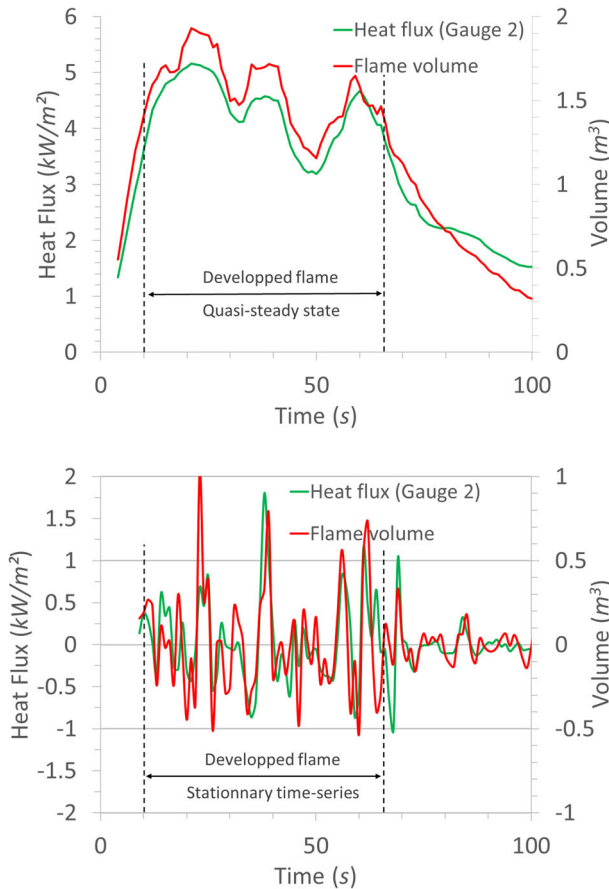


Figure 7. Decomposition into additive time series (Fire Test 2_2). Each raw time series (here flame volume and heat flux (Gauge 2)) can be expressed as a sum of (a) a trend component (7 s moving average) and (b) a fluctuating component (difference between raw and average signals).

cases) and significantly ($p < 0.001$) correlated to the flame radiation impinging at different locations ahead of the fire front.

Nevertheless, aspects relative to the spectral properties of the flame as a source of heat radiation must be discussed. The calibration of the heat flux transducers is performed using a source of infrared radiation with substantially all its radiation within the flat range of the spectral transmittance band of the sapphire window. The calibration consists of determining the responsivity of the gauges (in mV per kW/m²) because their output is proportional to the heat transfer rate. The calibration process may be questionable for applications in the presence of a flame because the spectral radiance of this black body reference is different from the emission spectrum of the flames. The flame emission spectrum shows high emission peaks attributed to combustion products (CO₂ and H₂O) and weak emissions from these bands rather than a continuous spectrum following Planck's law [71]. Thus, caution should be exercised when using derived relationships between flame volume and radiant heat flux in the presence of flames with unknown emission

Table 3
Correlation Matrix of the Fluctuations of Flame Geometric Variables and Radiant Heat Fluxes Measured at Different Locations, for the Full Set of Experiments

		Area	Volume	Heat flux 1	Heat flux 2	Heat flux 3
Test 2_1	Volume	0.87***	1			
	Heat flux 1	0.69***	0.82***	1		
	Heat flux 2	0.66***	0.75***	0.90***	1	
	Heat flux 3	0.59***	0.71***	0.72***	0.93***	1
	Heat flux 4	0.66***	0.76***	0.88***	0.93***	0.89***
Test 2_2	Volume	0.80***	1			
	Heat flux 1	0.70***	0.77***	1		
	Heat flux 2	0.66***	0.77***	0.96***	1	
	Heat flux 3	0.66***	0.78***	0.93***	0.99***	1
	Heat flux 4	0.70***	0.81***	0.94***	0.98***	0.98***
Test 4_1	Volume	0.87***	1			
	Heat flux 1	0.69***	0.82***	1		
	Heat flux 2	0.70***	0.85***	0.96***	1	
	Heat flux 3	0.64***	0.80***	0.87***	0.97***	1
	Heat flux 4	0.69***	0.83***	0.95***	0.98***	0.95***
Test 4_2	Volume	0.65***	1			
	Heat flux 1	0.37**	0.63***	1		
	Heat flux 2	0.42***	0.63***	0.95***	1	
	Heat flux 3	0.40***	0.59***	0.85***	0.96***	1
	Heat flux 4	0.47***	0.67***	0.90***	0.96***	0.93***
Test 8_1	Volume	0.74***	1			
	Heat flux 1	0.55***	0.68***	1		
	Heat flux 2	0.66***	0.75***	0.90***	1	
	Heat flux 3	0.59***	0.71***	0.72***	0.93***	1
	Heat flux 4	0.66***	0.76***	0.88***	0.93***	0.89***

***Correlation is significant at the 0.001 level, **correlation is significant at the 0.05 level

properties. For instance, the linear relationship could be qualitatively identical but with a different slope depending on the soot production (optically thin or optically thick flames), or if the flame at the same temperature emits radiation according to a different range of wavelengths, or if the peaks of the radiation emission are partly attenuated by the presence of smoke.

The previous results confirm the validity of flame volume as a potential surrogate for the estimation of fire thermal properties. Nevertheless, some limitations exist. The fire pixel segmentation is crucial step of the method but the use of dual spectral band cameras enhanced significantly fire pixel detection. The flame reconstruction can't be performed in real-time and it took less than 10 min for a desktop PC to perform the 3D reconstruction of an unsteady flame from 200 images. It should also be pointed out that the flame-volume based method is applicable only to fire scenarios where flames are mainly buoyancy-driven. Indeed, in case of strong wind conditions, the impingement of the stretch flames on the vegetation can prevent the accurate measurement of the flame volume and subsequent estimation of radiation field. More work is nevertheless required on a wider range of configurations than those considered in the present study (line of fire with different lengths or widths) before the technique can be used at a larger scale. First, the system requires further validation on a spreading fire front by experiments that implement a varying distance between the fire and each pair of cameras. The 3D reconstruction of the flame necessitates at least two synchronized stereovision systems that capture images from both the front and rear perspectives. The main weakness of the actual system mounted on tripods is that it is hard to deploy in poorly accessible terrain. Work is currently being accomplished on the integration of stereovision systems on unmanned aerial vehicles.

4. Conclusion

An image-based diagnostic system was developed for the 3D reconstruction of a flame front in the field. The image processing technique was tested on static line configurations at an intermediate scale (10 m^2). Although the range of experiments conducted over fuel beds is the relatively narrow, the preliminary results are promising. The flame volume is the variable that best describes flame radiation impinging ahead of a fire front. The linear relationship (and good correlations) between some flame geometric properties and heat fluxes indicates that the system consistently provides good estimations of flame features.

The main merit of this system lies in its ability to be deployed in any field configuration since no landmark on the terrain is required. The cameras don't need a particular pre-fire positioning provided that images of the flame front are recorded from complementary viewpoints. The inter-camera distance (baseline length) and focal length of the stereovision pairs have to be set in accordance to the distance to fire for lesser disparity errors. The system can be embedded into any motor or flying vehicles (cars, planes, helicopters, drones, etc.) provided that the cameras are georeferenced with a precision GPS. Considering the difficulty of thermal data collection in the presence of fire in the open, flame volume measurements can

therefore be used as a robust substitute for estimating, at a safe distance, the radiation fields. The flame features analysis is likely to play, in the near future, a greater role towards better characterization of the spread of fires, evaluation of the hazards or assistance for fire management activities.

References

1. Finney MA (2005) The challenge of quantitative risk analysis for wildland fire. *For Ecol Manag* 211(1):97–108. <https://doi.org/10.1016/j.foreco.2005.02.010>
2. Calkin DE, Gebert KM, Jones JG, Neilson RP (2005) Forest service large fire area burned and suppression expenditure trends. *J For* 103:179–183. <https://doi.org/10.1038/ncomms8537>
3. Jolly WM, Cochrane MA, Freeborn PH, Holden ZA, Brown TJ, Williamson GJ, Bowman DM (2015) Climate-induced variations in global wildfire danger from 1979 to 2013. *Nat Commun* 6:7537
4. Scott AC (2018) *Burning planet: the story of fire through time*. Oxford University Press, Oxford
5. Gómez-González S, Ojeda F, Fernandes PM (2018) Portugal and Chile: longing for sustainable forestry while rising from the ashes. *Environ Sci Policy* 81:104–107. <https://doi.org/10.1016/j.envsci.2017.11.006>
6. USDA (2018) Thomas burned area report, FS-2500-8. United States Department of Agriculture Forest Service, Washington
7. Campbell R (2018) U.S. firefighter injuries on the fireground, 2010–2014. *Fire Technol* 54(2):461–477. <https://doi.org/10.1007/s10694-017-0692-9>
8. Page WG, Butler BW (2018) Fuel and topographic influences on wildland firefighter turnover fatalities in Southern California. *Int J Wildland Fire* 27(3):141–154. <https://doi.org/10.1071/WF17147>
9. Lahaye S, Curt T, Fréjaville T, Sharples J, Paradis L, Hély C (2018) What are the drivers of dangerous fires in mediterranean France?. *Int J Wildland Fire* 27(3):155–163. <https://doi.org/10.1071/WF17087>
10. Pellegrini AFA, Ahlström A, Hobbie SE, Reich PB, Nieradzik LP, Staver AC, Scharenbroch BC, Jumpponen A, Anderegg WRL, Randerson JT, Jackson RB (2017) Fire frequency drives decadal changes in soil carbon and nitrogen and ecosystem productivity. *Nature* 553:194. <https://doi.org/10.1038/nature24668>
11. Larsen AE, Reich BJ, Ruminski M, Rappold AG (2017) Impacts of fire smoke plumes on regional air quality, 2006–2013. *J Expo Sci Environ Epidemiol* . <https://doi.org/10.1038/s41370-017-0013-x>
12. Hallema DW, Sun G, Caldwell PV, Norman SP, Cohen EC, Liu Y, Bladon KD, McNulty SG (2018) Burned forests impact water supplies. *Nat Commun* 9(1):1307. <https://doi.org/10.1038/s41467-018-03735-6>
13. Rust AJ, Hogue TS, Saxe S, McCray J (2018) Post-fire water-quality response in the western United States. *Int J Wildland Fire* 27(3):203–216. <https://doi.org/10.1071/WF17115>
14. Stechishen E, Little EC (1971) Water application depths required for extinguishment of low-intensity fires in forest fuels, Canadian Forestry Service, Forest Fire Research Institute, Information Report FF-X-29. Ottawa
15. Andrews PL, Rothermel RC (1982) Charts for interpreting wildland fire behaviour characteristics, USDA Forest Service, Intermountain Forest and Range Experiment Station, General Technical Report INT-131. Ogden

16. Alexander ME (2000) Fire behaviour as a factor in forest and rural fire suppression. New Zealand Fire Service Commission and The National Rural Fire Authority Forest Research Bulletin Number 197, Forest and Rural Fire Scientific and Technical Series Report Number 5. Wellington
17. Pérez Y, Pastor E, Planas E, Plucinski M, Gould J (2011) Computing forest fires aerial suppression effectiveness by IR monitoring. *Fire Saf J* 46(1):2–8. <https://doi.org/10.1016/j.firesaf.2010.06.004>
18. Hansen R (2012) Estimating the amount of water required to extinguish wildfires under different conditions and in various fuel types. *Int J Wildland Fire* 21(5):525–536. <https://doi.org/10.1071/WF11022>
19. Plucinski MP, Sullivan AL, Hurley RJ (2017) A methodology for comparing the relative effectiveness of suppressant enhancers designed for the direct attack of wildfires. *Fire Saf J* 87:71–79. <https://doi.org/10.1016/j.firesaf.2016.12.005>
20. Huggett C Oxygen consumption calorimetry. In: Fall technical meeting on chemical and physical processes in combustion. Combustion institute, eastern states section, Pittsburgh, 1978
21. Morandini F, Perez-Ramirez Y, Tihay V, Santoni P-A, Barboni T (2013) Radiant, convective and heat release characterization of vegetation fire. *Int J Therm Sci* 70:83–91. <https://doi.org/10.1016/j.ijthermalsci.2013.03.011>
22. Tihay V, Morandini F, Santoni P-A, Perez-Ramirez Y, Barboni T (2014) Combustion of forest litters under slope conditions: burning rate, heat release rate, convective and radiant fractions for different loads. *Combust Flame* 161(12):3237–3248. <https://doi.org/10.1016/j.combustflame.2014.06.003>
23. Fu TT (1974) Heat radiation from fires of aviation fuels. *Fire Technol* 10(1):54–67. <https://doi.org/10.1007/bf02590512>
24. Tewarson A (1980) Heat release rate in fires. *Fire Mater* 4(4):185–191. <https://doi.org/10.1002/fam.810040405>
25. Morandini F, Silvani X (2010) Experimental investigation of the physical mechanisms governing the spread of wildfires. *Int J Wildland Fire* 19(5):570–582. <https://doi.org/10.1071/WF08113>
26. Wan H, Gao Z, Ji J, Sun J, Zhang Y, Li K (2018) Predicting heat fluxes received by horizontal targets from two buoyant turbulent diffusion flames of propane burning in still air. *Combust Flame* 190:260–269. <https://doi.org/10.1016/j.combustflame.2017.12.003>
27. Byram GM (1959) Combustion of forest fuels. In: Davis KP (ed) *Forest fire: control and use* McGraw-Hill, New York, pp 61–89
28. Alexander ME, Cruz MG (2012) Interdependencies between flame length and fireline intensity in predicting crown fire initiation and crown scorch height. *Int J Wildland Fire* 21(2):95–113. <https://doi.org/10.1071/WF11001>
29. Thomas PH, Webster CT, Raftery MM (1961) Some experiments on buoyant diffusion flames. *Combust Flame* 5:359–367. [https://doi.org/10.1016/0010-2180\(61\)90117-1](https://doi.org/10.1016/0010-2180(61)90117-1)
30. Zukoski EE, Kubota T, Cetegen B (1981) Entrainment in fire plumes. *Fire Saf J* 3(3):107–121. [https://doi.org/10.1016/0379-7112\(81\)90037-0](https://doi.org/10.1016/0379-7112(81)90037-0)
31. Heskestad G (1983) Luminous heights of turbulent diffusion flames. *Fire Saf J* 5(2):103–108. [https://doi.org/10.1016/0379-7112\(83\)90002-4](https://doi.org/10.1016/0379-7112(83)90002-4)
32. Cox G, Chitty R (1985) Some Source-Dependent effects of unbounded fires. *Combust Flame* 60(3):219–232. [https://doi.org/10.1016/0010-2180\(85\)90027-6](https://doi.org/10.1016/0010-2180(85)90027-6)
33. Heskestad G (2016) Fire plumes, flame height, and air entrainment. In: Hurley MJ (ed) *SFPE handbook of fire protection engineering*. Springer, New York, pp 396–428. <https://doi.org/10.1007/978-1-4939-2565-0>

34. Maynard TB, Butta JW (2018) A physical model for flame height intermittency. *Fire Technol* 54(1):135–161. <https://doi.org/10.1007/s10694-017-0678-7>
35. Li K, Mao S, Feng R (2018) Estimation of heat release rate and fuel type of circular pool fires using inverse modelling based on image recognition technique. *Fire Technol* . <https://doi.org/10.1007/s10694-018-0795-y>
36. Butler B, Cohen J (1998) Firefighter safety zones: a theoretical model based on radiative heating. *Int J Wildland Fire* 8(2):73–77. <https://doi.org/10.1071/WF9980073>
37. Zárate L, Arnaldos J, Casal J (2008) Establishing safety distances for wildland fires. *Fire Saf J* 43(8):565–575. <https://doi.org/10.1016/j.firesaf.2008.01.001>
38. Rossi JL, Simeoni A, Moretti B, Leroy-Cancellieri V (2011) An analytical model based on radiative heating for the determination of safety distances for wildland fires. *Fire Saf J* 46(8):520–527. <https://doi.org/10.1016/j.firesaf.2011.07.007>
39. Sudheer S, Kumar L, Manjunath BS, Pasi A, Meenakshi G, Prabhu SV (2013) Fire safety distances for open pool fires. *Infrared Phys Technol* 61:265–273. <https://doi.org/10.1016/j.infrared.2013.09.006>
40. Butler BW (2014) Wildland firefighter safety zones: a review of past science and summary of future needs. *Int J Wildland Fire* 23(3):295–308. <https://doi.org/10.1071/WF13021>
41. Beyler CL (2016) Fire hazard calculations for large, open hydrocarbon fires. *SFPE handbook of fire protection engineering*, vol III. Fifth edn. Springer, New York, pp 2591–2663
42. Zhou K, Liu N, Zhang L, Satoh K (2014) Thermal radiation from fire whirls: revised solid flame model. *Fire Technol* 50(6):1573–1587. <https://doi.org/10.1007/s10694-013-0360-7>
43. Wang J-W, Fang J, Guan J-F, Zeng Y, Zhang Y-M (2016) Flame volume and radiant fraction of jet diffusion methane flame at sub-atmospheric pressures. *Fuel* 167:82–88. <https://doi.org/10.1016/j.fuel.2015.11.049>
44. Wang P, Liu N, Bai Y, Zhang L, Satoh K, Liu X (2017) An experimental study on thermal radiation of fire whirl. *Int J Wildland Fire* 26(8):693–705. <https://doi.org/10.1071/WF17010>
45. Fang J, Wang J, Tu R, Shang R, Y-m Zhang, J-j Wang (2018) Optical thickness of emissivity for pool fire radiation. *Int J Therm Sci* 124:338–343. <https://doi.org/10.1016/j.ijthermalsci.2017.10.023>
46. Shen G, Zhou K, Wu F, Jiang J, Dou Z (2019) A model considering the flame volume for prediction of thermal radiation from pool fire. *Fire Technol* 55(1):129–148. <https://doi.org/10.1007/s10694-018-0779-y>
47. Marbach G, Loeffe M, Brupbacher T (2006) An image processing technique for fire detection in video images. *Fire Saf J* 41(4):285–289. <https://doi.org/10.1016/j.firesaf.2006.02.001>
48. Ko B, Cheong K-H, Nam J-Y (2010) Early fire detection algorithm based on irregular patterns of flames and hierarchical Bayesian networks. *Fire Saf J* 45(4):262–270. <https://doi.org/10.1016/j.firesaf.2010.04.001>
49. Matthews S, Sullivan A, Gould J, Hurley R, Ellis P, Larmour J (2012) Field evaluation of two image-based wildland fire detection systems. *Fire Saf J* 47:54–61. <https://doi.org/10.1016/j.firesaf.2011.11.001>
50. Emmy Prema C, Vinsley SS, Suresh S (2018) Efficient flame detection based on static and dynamic texture analysis in forest fire detection. *Fire Technol* 54(1):255–288. <https://doi.org/10.1007/s10694-017-0683-x>
51. Raj VC, Prabhu SV (2018) Measurement of geometric and radiative properties of heptane pool fires. *Fire Saf J* 96:13–26. <https://doi.org/10.1016/j.firesaf.2017.12.003>

52. Le Maoult Y, Sentenac T, Orteu JJ, Arcens JP (2007) Fire detection: a new approach based on a low cost CCD camera in the near infrared. *Process Saf Environ Protect* 85(3):193–206. <https://doi.org/10.1205/psep06035>
53. Toulouse T, Rossi L, Akhloufi MA, Pieri A, Maldague X (2018) A multimodal 3D framework for fire characteristics estimation. *Meas Sci Technol* 29(2):025404. <https://doi.org/10.1088/1361-6501/aa9cf3>
54. Burnett JD, Wing MG (2018) A low-cost near-infrared digital camera for fire detection and monitoring. *Int J Remote Sens* 39(3):741–753. <https://doi.org/10.1080/01431161.2017.1385109>
55. Mason PS, Fleischmann CM, Rogers CB, McKinnon AE, Unsworth K, Spearpoint M (2009) Estimating thermal radiation fields from 3D flame reconstruction. *Fire Technol* 45(1):1–22. <https://doi.org/10.1007/s10694-008-0041-0>
56. Xin Y (2014) Estimation of chemical heat release rate in rack storage fires based on flame volume. *Fire Saf J* 63:29–36. <https://doi.org/10.1016/j.firesaf.2013.11.004>
57. Hu L, Zhang X, Wang Q, Palacios A (2015) Flame size and volumetric heat release rate of turbulent buoyant jet diffusion flames in normal- and a sub-atmospheric pressure. *Fuel* 150:278–287. <https://doi.org/10.1016/j.fuel.2015.01.081>
58. Beji T, Verstockt S, Zavaleta P, Merci B (2016) Flame spread monitoring and estimation of the heat release rate from a cable tray fire using video fire analysis (VFA). *Fire Technol* 52(3):611–621. <https://doi.org/10.1007/s10694-015-0538-2>
59. de Ris J (1979) Fire radiation—A review. *Symp (Int) Combust* 17 (1):1003–1016. doi:[https://doi.org/10.1016/S0082-0784\(79\)80097-1](https://doi.org/10.1016/S0082-0784(79)80097-1)
60. Wu Z, Zhou Z, Tian D, Wu W (2015) Reconstruction of three-dimensional flame with color temperature. *V Comput* 31(5):613–625. <https://doi.org/10.1007/s00371-014-0987-5>
61. Bheemul HC, Lu G, Yan Y (2002) Three-dimensional visualization and quantitative characterization of gaseous flames. *Meas Sci Technol* 13(10):1643–1650. <https://doi.org/10.1088/0957-0233/13/10/318>
62. Upton TD, Verhoeven DD, Hudgins DE (2011) High-resolution computed tomography of a turbulent reacting flow. *Exp Fluids* 50(1):125–134. <https://doi.org/10.1007/s00348-010-0900-6>
63. Silvani X, Morandini F (2009) Fire spread experiments in the field: temperature and heat fluxes measurements. *Fire Saf J* 44(2):279–285. <https://doi.org/10.1016/j.firesaf.2008.06.004>
64. Orloff L (1981) Simplified radiation modeling of pool fires. *Symp (Int) Combust* 18 (1):549–561. [https://doi.org/10.1016/S0082-0784\(81\)80060-4](https://doi.org/10.1016/S0082-0784(81)80060-4)
65. Ko Y-C, Hou S-S, Lin T-H (2005) Laminar diffusion flames in a multiport burner. *Combust Sci Technol* 177(8):1463–1484. <https://doi.org/10.1080/00102200590959323>
66. Knight IK, Sullivan AL (2004) A semi-transparent model of bushfire flames to predict radiant heat flux. *Int J Wildland Fire* 13(2):201–207. <https://doi.org/10.1071/WF03047>
67. Silvani X, Morandini F, Muzy J-F (2009) Wildfire spread experiments: fluctuations in thermal measurements. *Int Commun Heat Mass Transf* 36(9):887–892. <https://doi.org/10.1016/j.icheatmasstransfer.2009.06.008>
68. Thomas PH (1963) The size of flames from natural fires. *Symp (Int) Combust* 9 (1):844–859. [https://doi.org/10.1016/S0082-0784\(63\)80091-0](https://doi.org/10.1016/S0082-0784(63)80091-0)
69. Drysdale D (2011) An introduction to fire dynamics, 3rd edn. Wiley, Chichester
70. Weise DR, Fletcher TH, Cole W, Mahalingam S, Zhou X, Sun L, Li J (2018) Fire behavior in chaparral—Evaluating flame models with laboratory data. *Combust Flame* 191:500–512. <https://doi.org/10.1016/j.combustflame.2018.02.012>

71. Boulet P, Parent G, Acem Z, Collin A, Séro-Guillaume O (2011) On the emission of radiation by flames and corresponding absorption by vegetation in forest fires. *Fire Saf J* 46(1–2):21–26. <https://doi.org/10.1016/j.firesaf.2010.03.006>

Publisher's Note Springer Nature remains neutral with regard to jurisdictional claims in published maps and institutional affiliations.